Nanoscale Advances

ROYAL SOCIETY OF CHEMISTRY

PAPER

View Article Online
View Journal | View Issue

Cite this: *Nanoscale Adv.*, 2025, **7**, 7559

The role of the tin precursor in tuning TMS@carbon yolk–shell nanospheres for enhanced sulfur utilization

Catherine Sekyerebea Diko, †[a] Haodong Shi,†[b] Wang Lei,[a] Zichen Zhu,[c] Yining Liu,[c] Maurice Abitonze,[a] Wendolina Martina Micha Obono,[d] Yimin Zhu,*[a] Yan Yang, *[c] Zhongshuai Wu [b] and Jian Liu*[e]

Lithium–sulfur (Li–S) batteries are promising candidates for future energy storage systems because of their abundant theoretical capacity and low cost. However, challenges such as polysulfide shuttle effects and poor conductivity hinder their practical use. Yolk–shell structured nanocomposites offer a promising avenue for addressing the challenges in Li–S batteries. Herein, one-pot hydrothermal synthesis of yolk–shell SnS_2@MoS_2@C nanospheres is reported, where the inclusion of the tin precursor plays a pivotal role in tuning these unique nanostructures. The resulting architecture provides enlarged interlayer spacing, internal voids, and robust stability, facilitating efficient ion transport and volume buffering. Electrochemical evaluations reveal a high initial capacity of 1445 mA h g^{-1} at 0.1C, with excellent rate-performance, retaining 802 mA h g^{-1} at 3C. Remarkably, at 1C, the capacity increases from 1044.8 to 1114.6 mA h g^{-1} after 600 cycles. These results highlight the structural and functional advantages of SnS_2-driven yolk–shell architectures for next-generation Li–S cathodes.

Received 12th August 2025
Accepted 11th September 2025

DOI: 10.1039/d5na00772k

rsc.li/nanoscale-advances

1. Introduction

The growing need for sustainable energy technologies has intensified research efforts into advanced electrochemical storage applications.[1–4] Although lithium-ion batteries (LIBs) are widely used in consumer electronics and electric vehicles, they face resource limitations, safety concerns, and energy density constraints. Thus, there is a demand for the development of new materials that can deliver high-performance for energy storage.[5,6] In recent years, lithium–sulfur (Li–S) batteries have been particularly appealing due to their high theoretical energy density (~2600 W h kg^{-1}), cost-effectiveness, and abundance of sulfur.[7,8] However, their practical implementation is hindered by polysulfide shuttle effects, sluggish redox kinetics, and significant volume expansion during cycling, which lead to capacity fading and poor cycling stability.[9–11]

To address these limitations, the development of advanced electrode materials with tunable electrochemical properties is essential. Transition metal sulfides (TMSs) serve as promising electrode materials for energy storage applications. This is due to their high theoretical capacities, layered structures, and relatively low production costs.[12–14] However, the practical use of TMS faces limitations due to its low electronic and ionic conductivities and significant volume expansion during cycling. These issues cause electrode pulverization, detachment of active materials, and, eventually, rapid capacity fading with poor rate performance during repeated charge–discharge cycles.[14] To overcome these limitations, one approach involves constructing TMS composites where conductive carbon-based materials are adopted.[15,16] Another strategy focuses on engineering the shape and morphology of TMS materials at the nanoscale (nanoparticles, nanosheets, nanorods, nanospheres, *etc.*).[17] By harnessing these two approaches, TMS carbon-based composites can offer significant structural advantages and enhanced functionalities for advanced energy storage applications.

Recently, yolk–shell architectures have served as active materials in battery assembly, boosting energy density, while the void space relieves mechanical stress from volume changes, preventing structural damage.[18–20] When applied to Li–S batteries, this design can accommodate and confine soluble polysulfides within the shell. Also, yolk–shell hosts have been shown to accelerate polysulfide conversion by improving sulfur utilization and extending cycle life.[21] Despite these advances,

[a]*Environmental Science and Engineering, Dalian Maritime University, Environmental Science & Engineering College, 116026, China*

[b]*State Key Laboratory of Catalysis, Dalian Institute of Chemical Physics, Chinese Academy of Sciences, 457 Zhongshan Road, Dalian, Liaoning, China*

[c]*Research Department 11, SINOPEC (Dalian) Research Institute of Petroleum and Petrochemicals Co., Ltd, No. 96, Nankai Street, Lushunkou District, Dalian, 116045, Liaoning, China*

[d]*Materials Science and Engineering College, Dalian University of Technology, 116024, China*

[e]*College of Chemistry and Chemical Engineering, Inner Mongolia University, Hohhot, Inner Mongolia, People's Republic of China*

† These authors contributed equally to this paper.

the fabrication of yolk–shell TMS-carbon composites remains underexplored for Li–S applications.

In this study, a novel facile one-pot hydrothermal synthesis of yolk–shell SnS_2/MoS_2/Carbon (SnS_2@MoS_2@C) nanospheres was designed for Li–S applications. The incorporation of a tin (Sn) precursor was found to play a crucial role in regulating the nanosphere structure, promoting the formation of a porous yolk–shell with expanded interlayer architectures. Notably, in the absence of the Sn precursor, hollow-shell MoS_2@C nanospheres were obtained, whereas omitting both Sn and carbon precursors led to the formation of amorphous core–shell MoS_2 structures. Comprehensive characterization revealed that yolk–shell SnS_2@MoS_2@C exhibited uniform morphology, enhanced surface area, and expanded interlayer spacing for improved ion and electron transport. This design significantly enhances electrochemical performance by providing an abundance of active sites for sulfur redox reactions. The yolk–shell SnS_2@MoS_2@C nanospheres demonstrated superior lithium–sulfur redox kinetics, achieving a high discharge capacity of 1445 mA h g^{-1} at 0.1C and maintaining 802 mA h g^{-1} at 3C. Furthermore, the yolk–shell exhibited remarkable cycling stability, achieving a capacity of 1114.6 mA h g^{-1} at 1C after 600 cycles and a capacity increase rate of 0.01% per cycle. Compared to hollow-shell MoS_2@C and amorphous MoS_2 nanospheres, the yolk–shell nanostructure also suppressed the polysulfide shuttle more effectively and promoted stable cycling. These results show the efficacy of SnS_2-induced yolk–shell engineering as a promising method for designing high-performance cathode materials in lithium–sulfur battery systems.

2. Experimental details

2.1 Materials

Cetyltrimethylammonium bromide (CTAB, AR 99%) and ethanol (AR 99%) were purchased from the Chinese Medicine Group. Pluronic F127, L-cysteine (AR 98%), resorcinol (AR 99%), and 37 wt% formaldehyde solution were obtained from Sigma-Aldrich. Sodium molybdate dihydrate ($Na_2MoO_4 \cdot 2H_2O$, AR 99%) and sodium stannate trihydrate ($Na_2SnO_3 \cdot 3H_2O$, AR 99%) were purchased from Kermel. Deionized water was purified using a ThermoFisher Scientific Barnstead TII system.

2.2 Synthesis of yolk–shell SnS_2@MoS_2@C composite nanospheres

To synthesize the yolk–shell SnS_2@MoS_2@C composite nanospheres, 0.10 g of Pluronic F127, 0.26 g of CTAB, and 1.2 g of L-cysteine were completely dissolved in a 28% ethanol solution. The solution was stirred on a magnetic stirrer for 60 minutes at room temperature. After that, 0.05 g of $Na_2SnO_3 \cdot 3H_2O$ was added, followed by 0.25 g of $Na_2MoO_4 \cdot 2H_2O$ after 30 minutes. These two steps are interchangeable; however, complete dissolution in each step is vital. Subsequently, 0.2 g of resorcinol and 0.28 mL of formaldehyde (37%) were added to the mixture at the same time interval. Afterwards, the mixture was kept at 30 °C for 24 hours and then transferred to a Teflon-lined autoclave and subjected to hydrothermal treatment at 220 °C for 24 hours under static conditions. The SnS_2@MoS_2@RF product was centrifuged, washed three times with deionized water and ethanol, and dried under vacuum at 60 °C overnight.

For carbonization, the SnS_2@MoS_2@RF powder was heated in a tube furnace under a N_2 atmosphere. This involved an initial heating rate of 1 °C min^{-1} up to 220 °C with a dwell time of 60 minutes, followed by further heating at 1 °C min^{-1} to 400 °C maintained for 120 minutes to yield the final SnS_2@MoS_2@C yolk–shell nanospheres. This temperature was selected to ensure carbon formation while avoiding MoS_2 and SnS_2 decomposition.

2.3 Synthesis of MoS_2@C nanospheres

MoS_2@C nanospheres were synthesized following the same procedure and experimental conditions as SnS_2@MoS_2@C, but without the addition of $Na_2SnO_3 \cdot 3H_2O$.

2.4 Synthesis of MoS_2 nanospheres

MoS_2 nanospheres were also prepared under identical conditions to SnS_2@MoS_2@C, omitting $Na_2SnO_3 \cdot 3H_2O$, resorcinol, and formaldehyde from the precursor solution.

2.5 Material characterization

The morphological structures of the samples were observed using a standard and high-resolution JEOL JEM-2100F Transmission Electron Microscope (TEM and HRTEM) and a scanning electron microscope (SEM) with an accelerating voltage of 10 kV (Zeiss Supra 55, Germany). The phase/crystal structure of the samples was determined by X-ray diffraction (XRD) using Cu Kα radiation ($\lambda = 1.5406$ Å) over a 2θ range of 5–90° with a Smart-Lab diffractometer. The BET surface areas were measured using a Micromeritics ASAP 2460. Raman spectroscopy was performed using a HORIBA HR800. XPS analysis was performed using a K-ALPHA+ system, with the C 1s peak calibrated at 284.8 eV. The composition of the composite nanospheres was further determined by thermogravimetric analysis (TGA) using a METTLER TGA2. The analysis was performed from 25 °C to 900 °C in dry air at a heating rate of 5 °C min^{-1}. The specific surface area was determined by nitrogen adsorption/desorption using the Brunauer–Emmett–Teller (BET) method with a Micromeritics ASAP 2460 analyzer. Further determination of the elemental content was performed by using an ICP-OES: Agilent 5110.

2.6 Lithium polysulfide (LiPS) adsorption test

Sublimated sulfur and Li_2S were dissolved in 1,3-dioxolane (DOL) and 1,2-dimethoxymethane (DME) (v/v = 1 : 1) in a molar ratio of 5 : 1 to create a 10 mM Li_2S_6 solution. The mixture was heated and stirred at 65 °C until complete dissolution. Afterward, 10 mg of the nanomaterials were added to 5 mL of the Li_2S_6 solution and homogenized for 4 hours. The entire process was conducted within a glove box filled with argon. The color changes were observed by ultraviolet (UV) spectroscopy.

2.7 Preparation of the SnS_2@MoS_2@C cathode

The electrochemical performance of yolk–shell SnS_2@MoS_2@C nanospheres as the cathode material in lithium–sulfur (Li–S)

batteries was investigated. The procedure used was adapted from Lin *et al.*[22] To prepare the cathode, SnS_2@MoS_2@C was mixed with carbon black and polyvinylidene fluoride (PVDF) binder in a weight ratio of 70 : 20 : 10, and the mixture was homogenized in *N*-methyl-2-pyrrolidone (NMP) solvent to form a viscous cathode slurry. This slurry was then uniformly coated onto a 0.02 μm aluminum (Al) foil current collector and dried at 60 °C under vacuum for 12 hours.

2.8 Assembly of symmetric batteries for kinetic evaluation of polysulfide conversion

SnS_2@MoS_2@C electrodes served dual roles as both working and counter electrodes. 40 μL of catholyte (consisting of 0.5 mol L^{-1} Li_2S_6 and a 1.0 mol L^{-1} solution of LiTFSI with 1 wt% $LiNO_3$ in a 1 : 1 v/v mixture of DOL and DME) was added to each cathode. The cyclic voltammetry (CV) behaviors of the symmetric batteries were evaluated at a scan rate of 10 mV s^{-1}, with a voltage window spanning from −0.8 to 0.8 V.

2.9 Assembly and evaluation of Li–S coin cell batteries

First, Li_2S_8 catholyte was prepared in a molar ratio of 7 : 1 of sulfur and Li_2S dissolved in a 1 M lithium bis(trifluoromethanesulfonyl)imide (LiTFSI) electrolyte with 2 wt% lithium nitrate ($LiNO_3$) in 1,2-dimethoxyethane (DME) : 1,3-dioxolane (DOL) (1 : 1 v/v). The solution was heated to 70 °C and vigorously stirred to ensure complete sulfur dissolution. Li–S was assembled in an argon-filled glovebox with H_2O < 0.01 ppm and O_2 < 0.01 ppm in a typical assembly using CR2032 coin-type cells. 12 mm SnS_2@MoS_2@C coated on aluminum foil served as the cathode, and lithium foil served as the anode. Sulfur loading was maintained at ~1 mg cm^{-2} with a complementary electrolyte/sulfur ratio of 15 μL mg^{-1}. Also, a 19 mm Celgard 2400 was used as a separator. Ultimately, the electrochemical performance was evaluated using a Neware BTS 8.0 battery test system, in a voltage window of 1.7–2.8 V. Cyclic voltammetry (CV) and electrochemical impedance spectroscopy (EIS) were conducted on a CHI-760E electrochemical workstation at a scan rate of 0.1 mV s^{-1} to 0.5 mV s^{-1} and in the frequency range of 10 kHz to 0.01 Hz, respectively.

3. Results and discussion

Fig. 1a depicts the synthesis and mechanistic pathway of SnS_2@MoS_2@C yolk–shell nanospheres. The morphological properties of nanomaterials are reported to be influenced by initial precursor stoichiometry and reaction conditions.[23] To achieve this unique nanostructure, F127 and CTAB served as surfactants. In this way, CTAB stabilized the micelle formation while promoting spherical morphology. On the other hand, L-cysteine acted as a reducing agent and sulfur source to facilitate

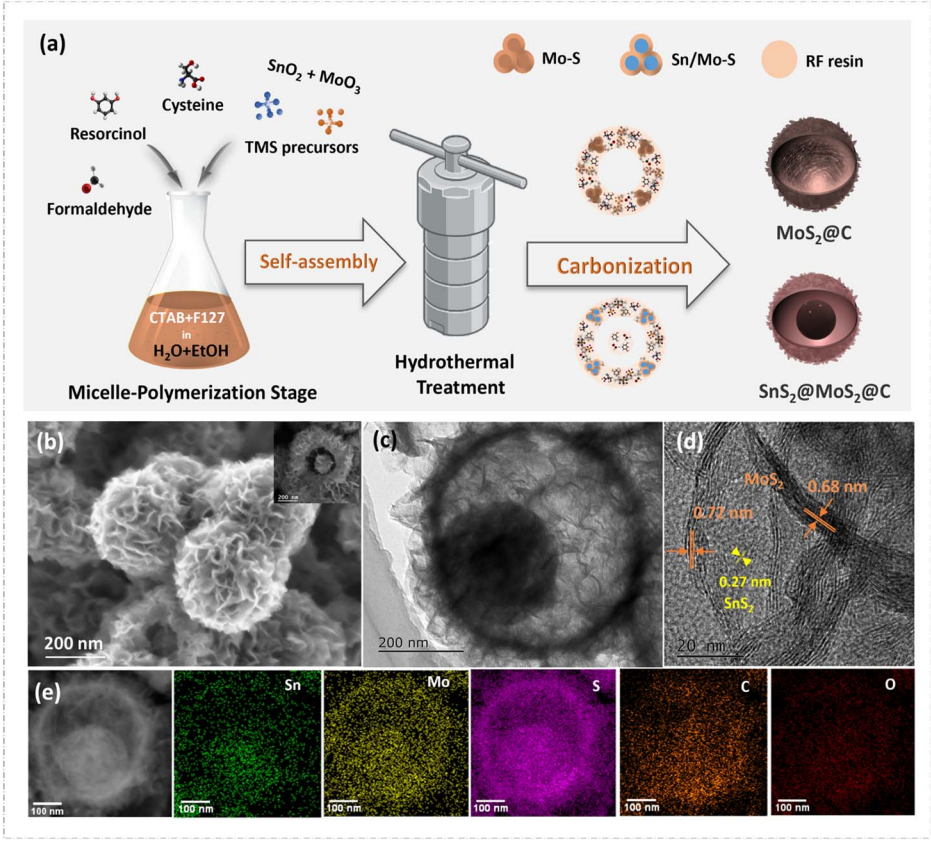

Fig. 1 (a) Schematic illustration of the synthesis and the possible mechanism of the formation of spherical SnS_2@MoS_2@C yolk–shell nanospheres through a one-pot self-assembly process. (b) SEM image and (c) TEM image. (d) HRTEM image showing 1T/2H-MoS_2 lattice fringes and SnS_2 planes and (e) TEM dark field and EDS-mapping of Sn, Mo, S, C, and O.

the reduction and ensure even distribution of Sn and Mo species. Moreover, the presence of Sn^{4+} triggered micelle separation to form a core–shell under static hydrothermal conditions within the resorcinol-formaldehyde (RF) framework. The resulting Sn-cysteine and Mo-cysteine complexes were decomposed during calcination to form SnS_2 and MoS_2 nanosheets integrated into carbon matrices within the yolk–shell nanostructures.

Simultaneously, carbonization of resorcinol-formaldehyde (RF) enhanced the porosity and structural stability of the nanospheres. Furthermore, the shell acted as a physical barrier to minimize polysulfide dissolution in lithium–sulfur batteries and a conductor for ion and electron transport.[24,25]

SEM images in Fig. 1b and S1a show the highly exposed composite edges of SnS_2@MoS_2 nanosheets uniformly and vertically grown onto a spherical yolk–shell matrix.[26] The TEM images in Fig. 1c and S1b further illustrate the porous nature of yolk–shell nanospheres. They displayed an average particle size of 410 nm. The average shell thickness and yolk size were measured to be 27 nm and 186 nm, respectively. This offered the necessary void spaces that can effectively confine polysulfides and enhance electrochemical performance.[27,28] To contextually understand the yolk–shell formation, SEM and TEM images of the control samples were compared side by side. As shown in Fig. S1c and d, without the addition of the Sn precursor, hollow-shell MoS_2@C microspheres were formed. The further absence of the RF precursor resulted in the formation of amorphous MoS_2 nanospheres (Fig. S1f and g). The diameter of MoS_2@C exhibited an average size of ~900 nm and a shell thickness of ~120 nm, while MoS_2 nanospheres exhibited ~600 nm overall. It is evident that the unique features exhibited in SnS_2@MoS_2@C yolk–shell nanospheres were synergically harnessed by the incorporation of the Sn precursor.

Compared to the control samples (Fig. S1e and i), the high-resolution TEM (HRTEM) image of SnS_2@MoS_2@C in Fig. 1d further displayed 1T/2H-MoS_2 crystalline and ordered nanosheets composed of a cross-linked interplanar spacing of about 0.68 nm and 0.72 nm corresponding to the (002) crystal plane.[29–32] A d-spacing of 0.27 nm was attributed to the (001) plane of SnS_2 nanosheets, which were displayed through the entire structural matrix.[33,34] Similar lattice fringes were observed by Liu *et al.* in the fabrication of a three-dimensional MoS_2/SnS_2-RGO anode for advanced sodium batteries and capacitors.[35] Also, the associated EDS mapping demonstrated the homogeneous distribution of tin (Sn), molybdenum (Mo), sulfur (S), carbon (C), and oxygen (O) elements within the yolk–shell composite nanospheres (Fig. 1e and S2c). For further clarity and as evidence of the elemental distribution, Fig. S2a and b present the yolk–shell nanostructure with matching cross-sectional morphology of SnS_2@MoS_2@C nanospheres.

The crystal structures of SnS_2@MoS_2@C nanospheres and its controls were also subjected to XRD analysis, as shown in Fig. 2a. The samples again displayed mostly 1T/2H-MoS_2 (JCPDS no. 37-1492) diffraction peaks indexed to 17.8° (002), 33.3° (100), and 58.5° (110) planes.[36,37] The diffraction peaks corresponding to MoS_2 in SnS_2@MoS_2@C were notably sharper and more intense than those in MoS_2@C. This indicates enhanced crystallinity and reduced amorphous content in the composite while promoting better ordering of the MoS_2 phase.[38] Also, the improvement can be attributed to the incorporation and uniform distribution of SnS_2, as confirmed by HRTEM and EDS-mapping. In contrast, the weaker peaks observed in bare MoS_2 can be ascribed to the poor transition from amorphous or less ordered Mo–S to the oriented MoS_2 layer.[39,40]

These structural modifications are consistent with the observed shifts in the Raman spectra (Fig. 2b). Also, 1T and 2H

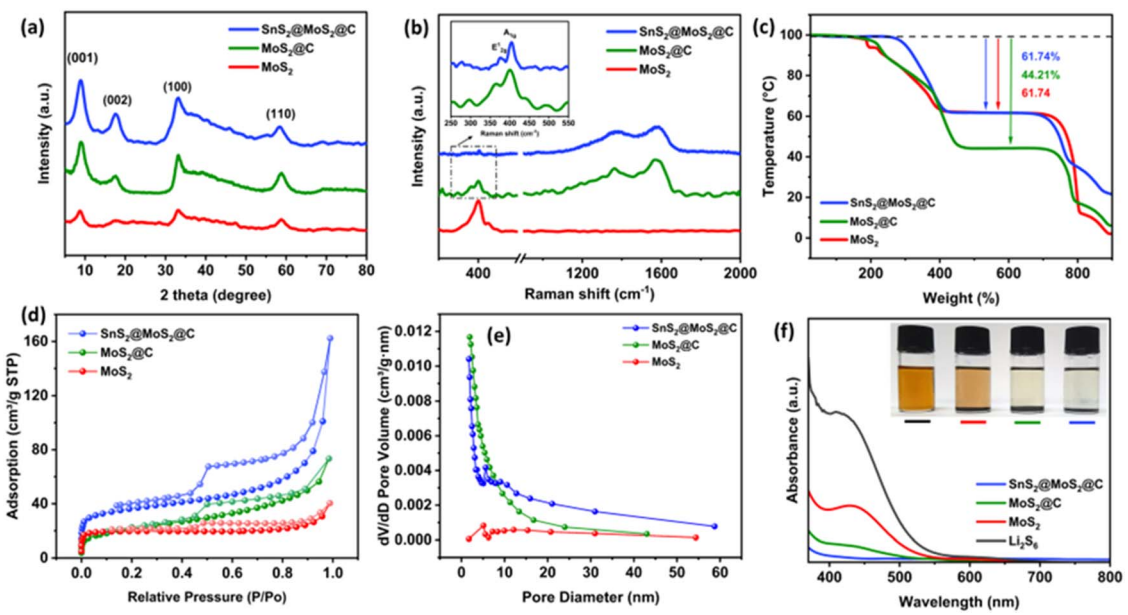

Fig. 2 (a) XRD patterns, (b) Raman spectra, (c) nitrogen adsorption–desorption isotherms, (d) corresponding pore size distribution, (e) TGA curve and (f) UV-vis absorption spectra of Li_2S_6 solution (the inset shows the visualized adsorption in Li_2S_6 solution after standing for four hours) of SnS_2@MoS_2@C, MoS_2@C, and MoS_2.

phases existed in SnS_2@MoS_2@C and MoS_2@C nanocomposites with E2g1 and A_{1g} modes of the hexagonal MoS_2 crystal.[41–43] MoS_2@C showed characteristic peaks at 365 and 400 cm^{-1}, while SnS_2@MoS_2@C moved to a slightly higher frequency with lower intensity peaks at 376 and 406 cm^{-1}, respectively. This shift, along with the reduction in peak intensity in SnS_2@MoS_2@C, could be attributed to defect formation and altered interlayer interactions resulting from the integration of SnS_2. Moreover, the relative intensity of I_D/I_G was calculated to be 0.86, suggesting a relatively high degree of graphitization.[44] From these observations, it is obvious that MoS_2 is the major species in the composite. Although SnS_2 plays a critical role in the formation of yolk–shell nanospheres and is uniformly distributed throughout the composite, its presence is almost undetectable by XRD and Raman spectroscopy. This is due to its relatively low concentration of the Sn precursor and strong signals from MoS_2. Evidently, these observations are consistent with reports on low-loading heterostructures (*e.g.*, SnS_2/Bi_2WO_6,[45] and MoS_2/SnS_2 (ref. 46 and 47)). Furthermore, the reduced Raman signals in the yolk–shell nanospheres can be an indication that SnS_2 and MoS_2 exist as few-layer or highly dispersed within the carbon matrix.[48,49]

Based on the TGA curves (Fig. 2c), between 25 °C and 120 °C, there was minimal mass loss attributed to the residual water adsorbed in the samples.[50] After an initial weight loss occurs at around 430 °C, the SnS_2@MoS_2@C composite retained 61.74% of its original weight, due to sulfur loss occurring between 100 and 430 °C. This weight reduction was primarily due to the combustion of carbon, the oxidation of MoS_2 to MoO_3, and the transformation of SnS_2 into SnO_2. An additional 24.66% weight loss occurred after the plateau between 700 and 800 °C, credited to continued MoS_2 oxidation and MoO_3 sublimation. In comparison, hollow-shell MoS_2@C retained 44.21% of its weight at a lower plateau. On the other hand, pure MoS_2 reported similar initial weight loss to SnS_2@MoS_2@C. The final weight drop beyond 800 °C in all samples corresponded to MoO_3 volatilization. Consequently, SnS_2@MoS_2@C retains 21.5% mass at 900 °C, compared to 10.6% for MoS_2@C and 1.5% for MoS_2.

As calculated by ICP (Table S2), the contents of SnS_2 and MoS_2 in SnS_2@MoS_2@C were estimated to be 9.77% and 64.48%, respectively. Similarly, MoS_2@C contained 46.8% of MoS_2. These findings are in close agreement with the TGA results and suggest that the weight loss was mainly due to the MoS_2 fraction. The additional 10.9% residue in SnS_2@MoS_2@C relative to MoS_2@C also aligns well with the SnS_2 fraction, confirming that the formation of SnO_2 accounted for the greater thermal stability.

The specific surface area of the nanospheres was calculated by BET analysis to ascertain the influence of SnS_2 on the ternary nanocomposite (Fig. 2d). Owing to the H3 hysteresis loop at a relative pressure of 0.4–0.9, all three samples exhibited type IV isotherms with mesoporous structures.[51–53] SnS_2@MoS_2@C exhibited the highest specific surface area of 124.34 $m^2\ g^{-1}$ and total pore volume (0.251 $cm^3\ g^{-1}$). This was greater than those of both MoS_2@C (75.95 $m^2\ g^{-1}$; 0.114 $cm^3\ g^{-1}$) and MoS_2 (61.86 $m^2\ g^{-1}$; 0.062 $cm^3\ g^{-1}$). As shown in Fig. 2e, SnS_2@MoS_2@C also exhibited a rich mesoporous distribution, with an average pore diameter of 8.08 nm, compared to MoS_2@C and MoS_2. These characteristics highlight the effectiveness of the yolk–shell structure of SnS_2@MoS_2@C to provide more accessible active sites and improved pore connectivity. Moreover, the large surface area could facilitate efficient adsorption of polysulfide intermediates, reduce the shuttle effect, and enhance the overall performance and lifespan of Li–S batteries.[54] This further suggests that the yolk–shell nanospheres stoichiometrically balance SnS_2/MoS_2 to enhance their surface properties for electrochemical applications.[51]

Further investigations were carried out to evaluate the efficacy of SnS_2@MoS_2@C in adsorbing Li polysulfides (LiPs) before electrochemical assessment. Fig. S3 details the presence of the synthesized nanomaterials in Li_2S_6 solution at time zero, and the inset of Fig. 2f depicts the adsorption performance. With the introduction of SnS_2@MoS_2@C and MoS_2@C, the Li_2S_6 solution was almost completely decolorized, while MoS_2 exhibited subtle alterations in color after standing for four hours inside a glovebox. The adsorption capability of SnS_2@MoS_2@C was further corroborated by ultraviolet-visible (UV-vis) spectroscopy, revealing the absence of absorbance peaks. This shows that SnS_2@MoS_2@C nanospheres have abundant specific surface area to facilitate the physical adsorption of Li polysulfides.

The chemical composition and states of the individual elements in the composite structures were also examined using XPS spectra. In Fig. 3a, the survey scan of SnS_2@MoS_2@C identified Sn, Mo, S, and C in the composite. The survey spectra of MoS_2@C and MoS_2 (Fig. S4a) showed Mo, S, and C signals. The C 1s signal in MoS_2 arose from residual organic matter. In Fig. 3b, the two peaks at 494.8 and 486.4 eV correspond to Sn $3d_{3/2}$ and Sn $3d_{5/2}$ binding energies (BE) of the SnS_2 state, respectively.[55,56] Fig. 3c also shows 1T and 2H phases of MoS_2 at around 229, 232, and 235 eV assigned to Mo $3d_{5/2}$, Mo $3d_{3/2}$ orbitals, and Mo^{6+}, similar to those of MoS_2@C and MoS_2 shown in Fig. S4b.[42,57] The peak at Mo^{6+} was ascribed to Mo–N bonding and matches the Mo_2N ($3p_{3/2}$) orbital, which may be caused by the Mo and N (Mo–N bond) coordination.[58]

Compared to MoS_2@C and MoS_2 in Fig. S4c, the yolk–shell was identified at peaks 162.5 and 163.6 eV, which correspond to S $2p_{3/2}$ and S $2p_{1/2}$ bonding, respectively. These were mainly ascribed to Mo–S $2p_{3/2}$ and Mo–S $2p_{1/2}$ of MoS_2 as shown in Fig. 3d.[59] The additional peak that appears at 161.58 eV resulted from the SnS_2 in the ternary yolk–shell nanospheres and was ascribed to Sn–S $2p_{1/2}$.[60] Fig. 3e identified three deconvoluted peaks in the C 1s spectrum. The peak at C–C (284.8 eV) was assigned to graphite carbon as the major species, and a weak peak of C–O resulted at 285.8 eV.[61,62] Additionally, the peak at 290.3 eV was assigned to O–C=C, inherited from the oxygen-containing precursors.[63,64] From the XPS elemental ratios (Table S3), SnS_2@MoS_2@C shows an S/Mo value of 2.66 and a Sn/Mo value of 0.20, indicating a sulfur-rich dual-sulfide system with clear Sn incorporation. In contrast, MoS_2@C exhibits a near-stoichiometric S/Mo ratio of 1.98, confirming the compositional differences that distinguish the two materials. The wt% also confirmed that SnS_2@MoS_2@C contained 7.6%

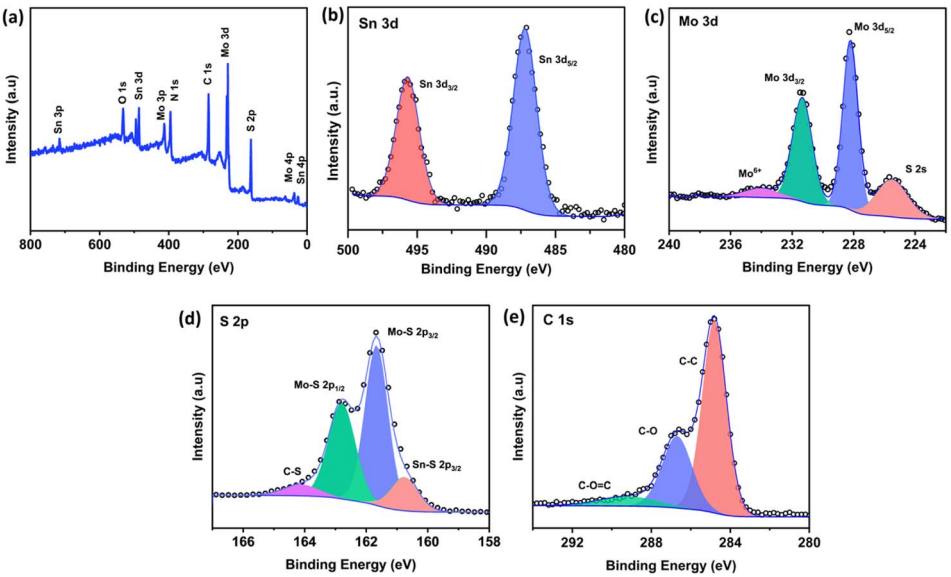

Fig. 3 (a) XPS survey scan and (b–e) corresponding high-resolution XPS spectra of Sn, Mo, S, and C elements of SnS_2@MoS_2@C.

Sn, 31.0% Mo, and 27.6% S, while MoS_2@C mainly has 32.6% Mo and 21.5% S without Sn, close to the ICP findings.

To gain insight into the electrochemical performance of the synthesized nanomaterials, the electrocatalytic performance of yolk–shell SnS_2@MoS_2@C and its controls was evaluated. These were carried out using Li_2S_6 in symmetric battery cells in the voltage range of −0.8 to 0.8 V (Fig. 4a). SnS_2@MoS_2@C exhibited the highest redox current of 0.14 V and the lowest polarization of −0.12 V, showing its superior polysulfide conversion and ion transport capabilities.[65,66] In contrast, MpmoS$_2$@C (a = 0.20 V, b = −0.21 V) and MoS_2 (a = 0.36 V, b = −0.26 V) displayed lower redox currents and higher polarization, indicating significantly reduced catalytic activity. Furthermore, the SnS_2@MoS_2@C cathode displayed the highest exchange current density in both reduction and oxidation processes that were fitted between (−0.2 and 0.2) V of the Tafel plot (Fig. S5a). It also showed the smallest Tafel slope extrapolated to obtain the I_0 value according to the Butler–Volmer equation.[67,68] Additionally, in the absence of Li_2S_6 in the electrolyte, a blunt-shaped CV curve was yielded (Fig. S5b). This suggests that the process is a chemical reaction rather than a capacitive behavior, making Li_2S_6 a unique electrochemically active species in the system.[69]

Cyclic voltammetry (CV) analysis conducted between 1.7 and 2.8 V revealed two cathodic peaks responsible for the multiple-step sulfur reduction process (Fig. 4b). The first cathodic peak 1 (C_1) was assigned to the transformation of S_8 into soluble long-chain lithium polysulfides (Li_2S_x, $4 \leq x \leq 8$). Again, further reduction to insoluble Li_2S_2/Li_2S was evidenced by the second cathodic peak 2 (C_2).[70] The anodic peak (A) was attributed to the reverse oxidation reaction of the short-chain sulfides to lithium polysulfides and then to sulfur. The SnS_2@MoS_2@C electrode displayed the most heightened peak currents and a larger peak area, an indication of the smaller polarization in the SnS_2@MoS_2@C battery.[71] The multiple redox pathways and enhanced reaction kinetics in SnS_2@MoS_2@C make it the optimal catalyst for battery applications. After four stable cycles of the CV test at 0.1 mV s^{-1} with good redox reversibility (Fig. S6a–c), SnS_2@MoS_2@C demonstrated the lowest charge transfer resistance (R_{ct}), as evidenced by the smallest semicircle in the Nyquist plot (Fig. 4c). The simulated interfacial impedance of the Li–S battery demonstrated a substantial reduction from 97.91 Ω to 45.47 Ω as the electrode material was changed from MoS_2 to SnS_2@MoS_2@C (Table S4). This decrease highlights the superior charge transfer efficiency and interfacial electrochemical activity of the SnS_2@MoS_2@C composite, outperforming MoS_2@C and MoS_2.[22] The results also significantly contribute to enhancing the battery performance of the SnS_2@MoS_2@C composite.

The corresponding Tafel slope analysis of the CV plot revealed that SnS_2@MoS_2@C exhibited significantly enhanced catalytic activity in both reduction and oxidation processes compared to MoS_2@C and MoS_2, as shown in Fig. 4d–f and the fitted Tafel slope in Fig. S7. The lower cathodic Tafel slope of SnS_2@MoS_2@C showed more efficient polysulfide conversion with reduced energy barriers. These improvements are attributed to its yolk–shell structure and the existence of SnS_2, and the thin, porous shell. Similarly, in the anodic process, SnS_2@MoS_2@C demonstrated superior charge transfer kinetics, further emphasizing the critical role of SnS_2 and yolk–shell engineering in facilitating redox reactions.

At different scan rates (0.1 to 0.5 mV s^{-1}), the peak currents of SnS_2@MoS_2@C showed increased slopes compared to MoS_2@C and MoS_2 (Fig. 4g–i). Furthermore, the linear fitting (Fig. 4j–l) and diffusion coefficient of lithium (D_{Li^+}) reflect the enhanced lithium polysulfide conversion kinetics of SnS_2@MoS_2@C compared to MoS_2@C and MoS_2 as calculated by using the Randles–Sevcik equation in Table S5. Thus, this suggests a faster Li^+ diffusion on the surface of yolk–shell morphology with the ability to synergistically modify the nanostructural properties.[72]

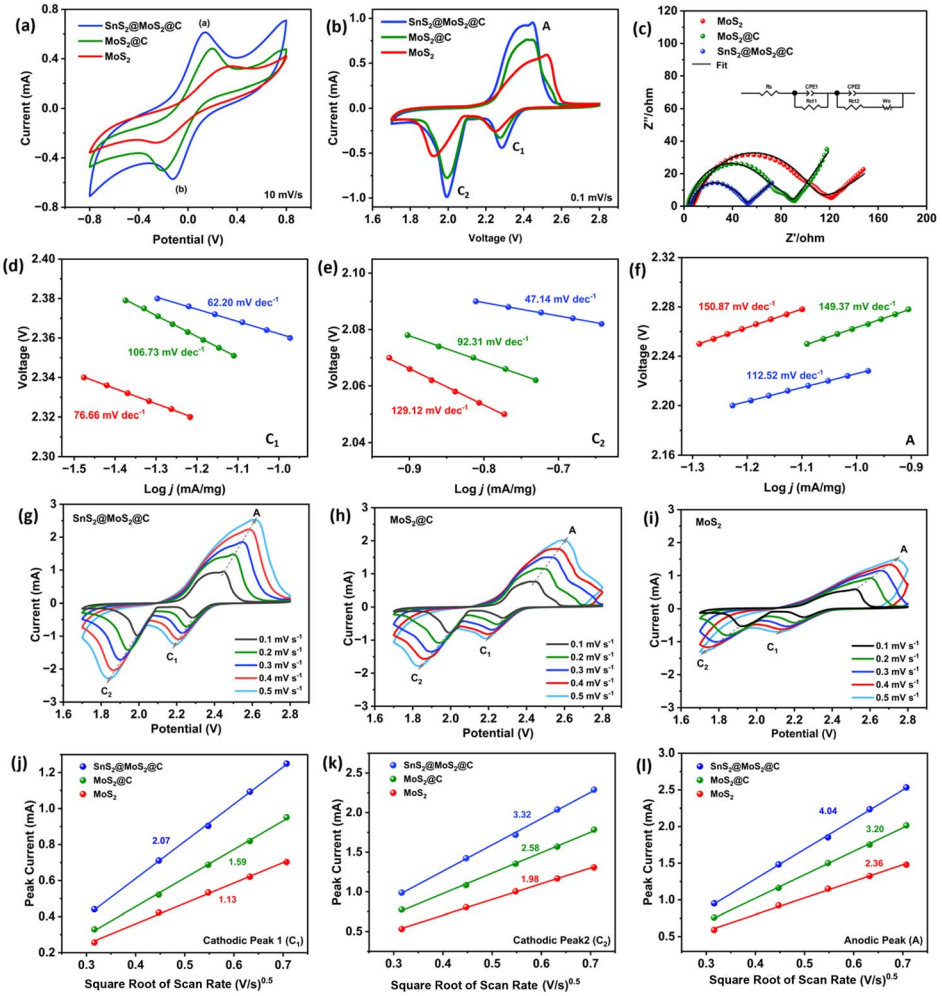

Fig. 4 (a) CV curves of the Li_2S_6 symmetric battery electrodes at 10 mV s^{-1}. (b) CV comparison profile of the electrodes as sulfur hosts at a scan rate of 0.1 mV s^{-1}. (c) Nyquist plots with fitted curves and the equivalent circuit model (the inset). (d–f) Corresponding Tafel plots of the CV curves at a scan rate of 0.1 mV s^{-1} of cathodic peak 1 (C_1), cathodic peak 2 (C_2), and anodic peak (A), respectively. (g–i) CV curves at different scan rates from 0.1 to 0.5 mV s^{-1}. (j–l) Corresponding Li^+ diffusion behavior analysis of SnS_2@MoS_2@C, MoS_2@C and MoS_2 electrodes.

The rate performance of the yolk–shell electrode was evaluated at different current rates (0.1–3C). As shown in Fig. 5a and S8a, SnS_2@MoS_2@C delivered the highest discharge capacities of 1445, 1340, 1184, 1092, 942, and 802 mA h g^{-1} at 0.1, 0.2, 0.5,1, 2, and 3C, respectively. When the current density returns to 0.1C, and then 0.2C, the discharge capacity bounced up to 1311 mA h g^{-1}, revealing a good stability rate.[73] In contrast, MoS_2@C and MoS_2 showed lower capacities at these current densities. MoS_2 especially revealed poor discharge capacities of 239 and 51 mA h g^{-1} at 2 and 3C, respectively. However, when returned to 0.1 and 0.2C, MoS_2@C and MoS_2 also showed discharge capacities with recoveries similar to their initial current densities. The corresponding charge/discharge curves of the batteries at different current rates are shown in Fig. S8b and c. In an overall observation, the discharge curves displayed two discharge plateaus with an increase in current density. However, in MoS_2, the discharge plateau became extremely short, and the voltage differences between charge and discharge plateaus widened. This is an indication of polarization at higher current densities, which is consistent with rate cycling performance. SnS_2@MoS_2@C, on the other hand, showed complete and wider plateaus of three discharge stages, thus providing discharge capacities with no deterioration even at higher current densities.

Fig. 5b further displayed the optimal performance of SnS_2@MoS_2@C yolk–shell nanospheres compared to MoS_2@C and MoS_2 through the initial charge/discharge evaluation of the electrodes at a current density of 0.1C. The enhanced polarization in SnS_2@MoS_2@C can be attributed to the effective synergistic integration of SnS_2 and MoS_2, which created additional active sites for redox reactions to accelerate lithium polysulfide conversion kinetics.[62] Furthermore, in Fig. 5c, the phase conversion coefficient (Q_H/Q_L) profile of SnS_2@MoS_2@C produced a higher coefficient of 2.46 than that of MoS_2@C (2.42) and MoS_2 (2.21). Here, Q_H is associated with the conversion process of S_8 to Li_2S_4, and Q_L with the conversion process of Li_2S_4 to Li_2S_2/Li_2S.[74] While all values are below the theoretical maximum of 3, they align with expected trends due to the

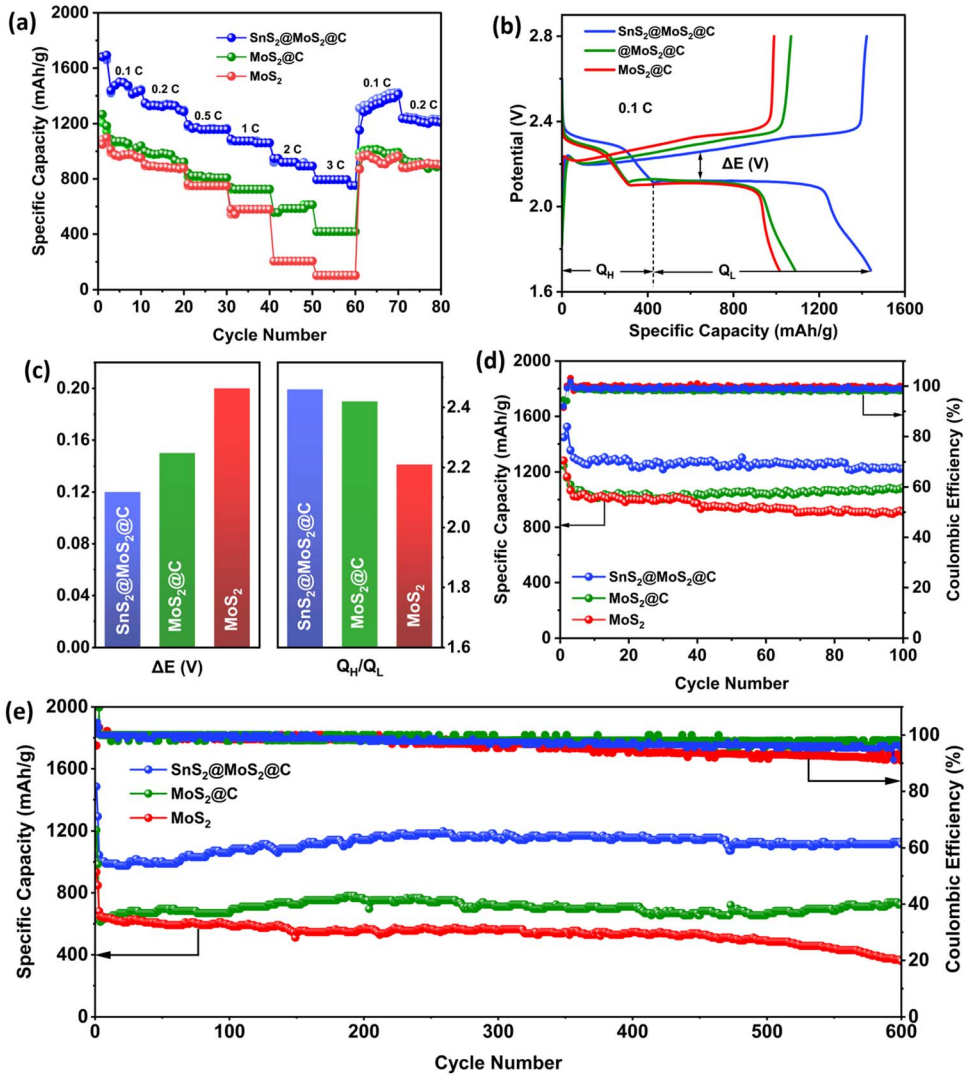

Fig. 5 (a) Rate performance, (b) discharging–charging profiles at 0.1C, (c) overpotentials (ΔE) and phase conversion coefficient (Q_H/Q_L) profiles, (d) cycling stability and coulombic efficiency at 0.2C after 100 cycles, and (e) long-term cycling stability and coulombic efficiency at 1C of SnS_2@MoS_2@C, MoS_2@C and MoS_2 Li–S batteries.

complex multi-electron transfer processes and the LiPS shuttle effect.[75,76] Additionally, their corresponding overpotentials (ΔE) revealed a linear decrease from 0.12 V, 0.15 V, and 0.20 V corresponding to SnS_2@MoS_2@C, MoS_2@C, and MoS_2, respectively. Ultimately, the differential capacity (dQ/dV) curves (Fig. S6d–f) and the corresponding charge/discharge profiles (Fig. S6g–i) of the cathode materials corroborated the cycling stability. Furthermore, the optimal electrochemical performance of SnS_2@MoS_2@C compared to the control sample during the first three cycles at 0.1C was consistent with the CV profile.

In terms of constant stability assessment, the SnS_2@MoS_2@C electrode displayed exceptional cycling stability and a coulombic efficiency (CE) of 98.75% at a current density of 0.2C, as shown in Fig. 5d and Table S6. It achieved an initial capacity of 1355.4 mA h g^{-1}, retaining 1224.6 mA h g^{-1} after 100 cycles, with a capacity fading rate of 0.097% per cycle. This performance highlights the robust structural integrity of the yolk–shell and its electrochemical stability. In contrast, the MoS_2@C electrode exhibited an initial capacity of 1108.0 mA h g^{-1}, which declined to 1089.0 mA h g^{-1} after 100 cycles. It also presented a higher fading rate of 0.26% per cycle. Meanwhile, the bare MoS_2 electrode, with an initial capacity of 1066.3 mA h g^{-1}, retained 897.2 mA h g^{-1}, displaying a fading rate of 0.15% per cycle. These results emphasize the superior performance of the SnS_2@MoS_2@C yolk–shell nanospheres, attributed to the synergistic interaction between SnS_2 and MoS_2 layers, which enhanced the interlayer spacing that aided ion transport while mitigating structural degradation.[62]

Furthermore, the yolk–shell SnS_2@MoS_2@C electrode demonstrated remarkable long-term cycle stability. The capacity increased from 1044.8 mA h g^{-1} to 1114.6 mA h g^{-1} over 600 cycles with a slight capacity increase of 0.01% and CE of 95.22% (Fig. 5e). This capacity increase could be attributed to

an activation process, where the electrode structure becomes more accessible to ions during extended cycling.[77,78] This characteristic could have led to improved utilization of active materials. In comparison, the MoS_2@C electrode showed a capacity improvement from 613 mA h g^{-1} to 724.6 mA h g^{-1}, which is a moderate structural improvement. The bare MoS_2 electrode suffered some capacity decay, decreasing from 680.71 mA h g^{-1} to 358.34 mA h g^{-1}, with a fading rate of 0.079% per cycle. To better demonstrate the performance advantages of the SnS_2@MoS_2@C yolk–shell nanospheres, the synthesis steps and electrochemical performance were compared with those of other highly studied TMS cathodes. As shown in Table S7, the SnS_2@MoS_2@C yolk–shell nanospheres outperformed most other electrodes in terms of rate capacities.

The remarkable cycling stability of SnS_2@MoS_2@C yolk–shell nanospheres stems from their structural and chemical features. The hollow interior provides sufficient space to buffer polysulfides during volume expansion, while the robust and porous shell preserves the framework. Elemental mapping confirmed that Sn, Mo, S, and C are uniformly distributed in both yolk and the shell, suggesting a cooperative role in structural integrity and electrochemical activity. Moreover, SnS_2 and MoS_2 possess a strong affinity for polysulfides, enabling strong adsorption that could confine the active material within the cathode. At the same time, the carbon layer physically confines them, thereby suppressing dissolution and shuttle effects over long-term cycling.

4. Conclusion

This study demonstrates the synthesis of SnS_2@MoS_2@C yolk–shell nanospheres *via* a simple one-pot hydrothermal method. The integration of the Sn precursor plays a key role in forming the yolk–shell structure, enhancing the properties of MoS_2@C by increasing the interlayer spacing and improving structural stability, which aids in polysulfide conversion. As a result, the yolk–shell composite exhibits exceptional discharge capacities of 1445 mA h g^{-1} at 0.1C and 802 mA h g^{-1} at 3C in Li–S batteries. After 600 cycles at 1C, it maintains a capacity of 1066 mA h g^{-1} with a coulombic efficiency of ~95.2%. The interaction between SnS_2 and MoS_2, coupled with the yolk–shell design, promotes efficient ion transport, reduces polarization, and enhances catalytic activity for polysulfide conversion. These results not only highlight the superior performance of SnS_2@MoS_2@C yolk–shell nanospheres in Li–S batteries but also provide a scalable strategy for designing advanced nanostructured composites for next-generation energy storage systems.

Author contributions

Catherine Sekyerebea Diko: conceptualization, data curation, formal analysis, visualization, writing-original draft, writing-review & editing. Haodong Shi: conceptualization, methodology. Wang Lei, Zichen Zhu, Yining Liu, Maurice Abitonze, and Wendolina Martina Micha Obono: data curation. Yimin Zhu, Zhongshuai Wu, and Jian Liu: supervision and reviewing. Yan Yang: conceptualization, reviewing, supervision, and funding acquisition.

Conflicts of interest

There are no conflicts to declare.

Data availability

All data supporting the findings of this study are available within the main manuscript and SI.

Supplementary information: additional structural characterizations (SEM, TEM, HRTEM, EDX, XPS), electrochemical analyses (CV, Tafel, EIS, charge/discharge), BET & ICP data, and comparative performance tables. See DOI: **https://doi.org/10.1039/d5na00772k**.

Acknowledgements

This work was supported financially by the National Key Research and Development Program of China (No. 2018YFE0181300), the National Natural Science Foundation of China (21905035), the Liaoning Revitalization Talents Program (XLYC1907093), and the Liaoning Natural Science Foundation (20180510043).

References

1 J. Sun, T. Wang, Y. Gao, Z. Pan, R. Hu and J. Wang, *InfoMat*, 2022, **4**, e12359.
2 F. Zhao, J. Xue, W. Shao, H. Yu, W. Huang and J. Xiao, *J. Energy Chem.*, 2023, **80**, 625–657.
3 F. O. Rourke, F. Boyle and A. Reynolds, *Renew. Sustain. Energy Rev.*, 2009, **13**, 1975–1984.
4 K. B. Karnauskas, S. L. Miller and A. C. Schapiro, *Geohealth*, 2020, **4**, e2019GH000237.
5 A. Mohammed, O. Saif, M. Abo-Adma, A. Fahmy and R. Elazab, *Sci. Rep.*, 2024, **14**, 283.
6 A. Jannesar Niri, G. A. Poelzer, S. E. Zhang, J. Rosenkranz, M. Pettersson and Y. Ghorbani, *Renew. Sustain. Energy Rev.*, 2024, **191**, 114176.
7 X. Judez, M. Martinez-Ibañez, A. Santiago, M. Armand, H. Zhang and C. Li, *J. Power Sources*, 2019, **438**, 226985.
8 Y. Li, J. G. Shapter, H. Cheng, G. Xu and G. Gao, *Particuology*, 2021, **58**, 1–15.
9 A. Raulo and G. Jalilvand, *Nano Energy*, 2024, **122**, 109265.
10 J. Cai, Y. Wu, Q. Wu, Z. Li, Z. Pan and L. Li, *J. Alloys Compd.*, 2022, **895**, 162594.
11 F. Liang, Y. Wang, Y. Wang, X. Zhang, J. Zhang and Q. Zhang, *Adv. Energy Mater.*, 2024, **14**, 2401959.
12 R. V. Bugga, S. C. Jones, J. Pasalic, C. S. Seu, J.-P. Jones and L. Torres, *J. Electrochem. Soc.*, 2017, **164**, A265–A276.
13 J. H. Zuo and Y. J. Gong, *Tungsten*, 2020, **2**, 134–146.
14 H. Wang, Y. Zhang, H. Ang, Y. Zhang, H. T. Tan and Y. Yu, *ACS Appl. Energy Mater.*, 2020, **3**, 11893–11899.
15 W. Zhu, J. Zhao and X. Tao, *J. Energy Storage*, 2024, **84**, 110934.

16 A. Pramanik, S. Sengupta, S. K. Saju, S. Chattopadhyay, M. Kundu and P. M. Ajayan, *Adv. Energy Mater.*, 2024, **14**, 2401657.
17 J. Rahmatinejad and Z. Ye, *Chem. Eng. J.*, 2024, **500**, 156872.
18 Q. Su, J. Zhang, Y. Wu and G. Du, *Carbon*, 2018, **140**, 433–440.
19 H. Wu, J. Li, Q. Ji and K. Ariga, *Sci. Technol. Adv. Mater.*, 2024, **25**, 2420664.
20 J. Wang, J. Liu, H. Zhou, P. He and C. Wang, *J. Appl. Electrochem.*, 2018, **48**, 509–518.
21 R. Bi, J. Zhao, M. Yang, J. Wang, R. Yu and D. Wang, *Inorg. Chem. Front.*, 2024, **11**, 8837–8846.
22 H. Lin, X. Wang, L. Yu, Y. Chen and J. Shi, *ACS Nano*, 2021, **15**, 17327–17336.
23 N. Baig, I. Kammakakam, W. Falath and I. Kammakakam, *Mater. Adv.*, 2021, **2**, 1821–1871.
24 H. Y. Seo, J. H. Choi, Y. B. Kim, J. S. Cho, Y. C. Kang and G. D. Park, *J. Mater. Chem. A*, 2023, **11**, 24738–24753.
25 Y. A. Chen, Y. T. Wang, H. S. Moon, K. Yong and Y. J. Hsu, *RSC Adv.*, 2021, **11**, 12288–12305.
26 Q. Zhang, X. Li, D. Li, G. Wu, X. Wang and Z. Jin, *Nano Res.*, 2016, **9**, 3038–3047.
27 X. Wang, Y. Wang, L. Yang, K. Wang, X. Lou and B. Cai, *J. Power Sources*, 2014, **262**, 72–78.
28 Y. Liu, S. Sun, J. Han, C. Gao, L. Fan and R. Guo, *Langmuir*, 2021, **37**, 2195–2204.
29 S. K. Park, S. H. Yu, S. Woo, B. Quan, D. C. Lee and Y. E. Sung, *CrystEngComm*, 2012, **14**, 8323–8325.
30 Z. Xu, J. Fang, J. Lu, D. He, S. He and Y. Luo, *iScience*, 2022, **25**, 104999.
31 H. Xiao, W. Zhang, G. Li, Z. Huang, J. Zhou and Z. Li, *Mater. Chem. Phys.*, 2017, **192**, 100–107.
32 K. Yao, Z. Xu, J. Huang, M. Ma, L. Fu and X. Shen, *Small*, 2019, **15**, 1805405.
33 H. Zhong, G. Yang, H. Song, Q. Liao, H. Cui and P. Shen, *J. Phys. Chem. C*, 2012, **116**, 9319–9326.
34 H. Li, X. Li, J. Zhao, J. Su, F. Huang and Q. Zhang, *Front. Chem.*, 2019, **7**, 339.
35 J. Liu, Y. G. Xu and L. B. Kong, *Solid State Ionics*, 2020, **355**, 115416.
36 X. Lin, K. Li, D. Wu, X. Luo, H. Liu and P. Liu, *Chem. Eng. J.*, 2019, **356**, 483–491.
37 J. Hu, Y. Xie, X. Zhou and Z. Zhang, *ACS Appl. Mater. Interfaces*, 2020, **12**, 1232–1240.
38 Y. Zhang, Z. Mu, J. Yang, Z. Yang, H. Zhang and Y. Lai, *Nanoscale Res. Lett.*, 2018, **13**, 287.
39 A. D. Marinov, A. T. Tesfaye, R. M. M. M. Ornelas, A. V. Silhanek, M. A. Susner and P. Samyn, *ACS Nano*, 2023, **17**, 5163–5186.
40 M. Krbal, J. Prikryl, V. Prokop, I. Pis, F. Bondino and A. V. Kolobov, *Appl. Phys. Lett.*, 2022, **121**, 193501.
41 N. Thi Xuyen and J. M. Ting, *Chem.–Eur. J.*, 2017, **23**, 17348–17355.
42 X. Zang, Y. Qin, T. Wang, F. Li, Q. Shao and N. Cao, *ACS Appl. Mater. Interfaces*, 2020, **12**, 55884–55893.
43 N. H. Attanayake, A. C. Thenuwara, A. Patra, Y. V. Aulin, T. M. Tran and D. R. Strongin, *ACS Energy Lett.*, 2018, **3**, 7–13.
44 H. Lim, H. Kim, S. O. Kim and W. Choi, *Chem. Eng. J.*, 2020, **387**, 124144.
45 Y. Xu, J. Yu, J. Long, L. Tu, W. Dai and L. Yang, *Nanomaterials*, 2022, **12**, 2030.
46 G. Ma, Z. Pan, Y. Liu, Y. Lu and Y. Tao, *Materials*, 2023, **16**, 4436.
47 W. Yu, Y. Wang, Y. Mei, Y. Zheng, T. Gao and F. Liang, *Adv. Sci.*, 2024, **11**, 2405135.
48 J. Quan, L. Lin, A. Y. Joe, E. G. Arnault, L. Zhao and T. F. Chung, *Nat. Mater.*, 2021, **20**, 1100–1105.
49 B. C. Windom, W. G. Sawyer and D. W. Hahn, *Tribol. Lett.*, 2011, **42**, 301–310.
50 H. Darjazi, A. Paolella, C. Gagnon, F. Vidal, A. Vijh and K. Zaghib, *Adv. Mater.*, 2024, **36**, 2313572.
51 S. Zhang, Z. Yin, L. Wang, M. Shu, X. Liang, S. Liang, L. Hu, C. Deng, K. Hu and X. Zhu, *Energy Mater.*, 2024, **4**, 400065.
52 Z. Jin, K. Xie, X. Hong and Z. Hu, *Chem. Eng. J.*, 2020, **394**, 124983.
53 Q. Sheng, Y. Wang, J. Zhang, J. Liu, F. Liu and Y. Tang, *J. Electroanal. Chem.*, 2023, **929**, 117119.
54 G. Mu, Z. He, X. Chen, Y. Chen, J. Li and D. Sun, *J. Colloid Interface Sci.*, 2025, **677**, 1–11.
55 M. Z. Ansari, N. Parveen, T. A. N. Peña, A. H. Ansari and S. A. Ansari, *Sci. Rep.*, 2019, **9**, 10225.
56 M. Jiang, T. Han and X. Zhang, *J. Colloid Interface Sci.*, 2021, **583**, 149–156.
57 H. Giang, T. T. T. Bui, D. H. Nguyen, Q. T. Tran and S. T. Nguyen, *Nanotechnology*, 2016, **27**, 225403.
58 N. Zhang, Z. Yang, W. Liu, F. Zhang and H. Yan, *Catalysts*, 2023, **13**, 90.
59 X. Yu, C. Chen, R. Li, T. Yang, W. Wang and Y. Dai, *J. Alloys Compd.*, 2022, **896**, 162784.
60 F. Liang, Y. Wang, Y. Wang, X. Zhang, J. Zhang and Q. Zhang, *Adv. Sci.*, 2024, **11**, 2306711.
61 K. Yuan, T. Hu, Y. Xu, R. Graf, P. A. van Aken and M. Forster, *Mater. Chem. Front.*, 2017, **1**, 278–285.
62 Y. Jiang, M. Wei, J. K. Feng, Y. C. Ma and S. L. Xiong, *ACS Appl. Mater. Interfaces*, 2017, **9**, 27697–27706.
63 N. Roy, S. Yasmin, A. K. Mohiuddin and S. Jeon, *Appl. Surf. Sci. Adv.*, 2023, **18**, 100517.
64 P. Lazar, R. Mach and M. Otyepka, *J. Phys. Chem. C*, 2019, **123**, 10695–10702.
65 J. Han, Y. Zhang, J. Wang, J. Li, Y. Tang and H. Wang, *ACS Appl. Nano Mater.*, 2024, **7**, 15015–15025.
66 Y. Bao, Y. Zhong, G. Zeng, Y. Chen, Y. Li and L. Li, *J. Colloid Interface Sci.*, 2025, **683**, 358–374.
67 A. Raveendran, M. Chandran and R. Dhanusuraman, *RSC Adv.*, 2023, **13**, 3843–3876.
68 Z. Lukács and T. Kristóf, *J. Electroanal. Chem.*, 2022, **918**, 116443.
69 D. Yang, C. Yao, Y. Liu, C. Luo, W. Zhang and S. Wei, *ACS Nano*, 2022, **16**, 11102–11114.
70 H. Lin, X. Wang, L. Yu, Y. Chen and J. Shi, *ACS Nano*, 2021, **15**, 17327–17336.
71 J. Zhang, Y. Wang, X. Zhang, F. Liang, Q. Zhang and Y. Wang, *Chem. Eng. J.*, 2023, **475**, 146009.

72 H. Wu, J. Li, Q. Ji and K. Ariga, *Sci. Technol. Adv. Mater.*, 2024, **25**, 2420664.
73 F. Li, J. Liu, G. Yang, S. Wei, X. Liu and Y. Gao, *J. Colloid Interface Sci.*, 2022, **626**, 535–543.
74 K. Kim, J. Kim and J. H. Moon, *Adv. Sci.*, 2023, **10**, 2206057.
75 R. Wang, J. Yang, X. Chen, Y. Zhao, W. Zhao and G. Qian, *Adv. Energy Mater.*, 2020, **10**, 1903550.
76 J. Luo, Y. Wu, J. Wang, J. Yu, L. Zhang and J. Zhu, *Chem. Eng. J.*, 2023, **451**, 138677.
77 L. Wu, J. Zhang, W. Zhou, S. Chen, J. Liu and S. Dai, *Nat. Commun.*, 2023, **14**, 1029.
78 E. Barcaro, V. Marangon, M. Mutarelli and J. Hassoun, *J. Power Sources*, 2024, **595**, 234059.